Towards long random sea simulations in numerical wave tanks

Eleni S. Zve and Johannes Spinneken
Department of Civil and Environmental Engineering, Imperial College London
London, United Kingdom

ABSTRACT

The present investigation concerns optimum wave absorption in numerical wave tanks. Recent developments have now established that (i) absorption controllers based on Infinite Impulse Response (IIR) filters are highly effective and (ii) cosh shaped wave board geometries offer significant potential in terms of active wave absorption due to their favourable added mass behaviour. While (i) and (ii) have been shown individually, their combination has never been demonstrated. To address this, a cosh shaped wavemaker is implemented in a time-domain numerical wave tank. Comparisons are presented between simple proportional controllers and the IIR approach, where the latter is demonstrated to offer excellent absorption performance over a very broad range of incident wave conditions. In excess of 90% amplitude (or equivalently 99% energy) absorption is demonstrated for the range $1 \leq kh \leq 8$, where k is the wavenumber and h is the water depth. A broad-banded absorption performance of this type covers the vast majority of wave components present in practical offshore wave spectra. Test cases are presented for both regular and irregular seas, paving the way towards numerical simulations of long random sea states. This paper focuses on a two-dimensional description of the problem. The approach adopted can also be extended to three dimensions, where reduced domain sizes (no sponge layer requirements) offer orders of magnitude improvement in terms of computational cost.

KEY WORDS: Absorbing wavemaker, Numerical wave tank, Optimum control, Force feedback

INTRODUCTION

Long random sea simulations are an essential part of laboratory model testing. This may, for example, concern the extreme wave crest statistics arising in steep sea states (Latheef & Swan 2013) or the loading of offshore structures (Rodríguez & Spinneken 2016). In either case, simulation times corresponding to 3 hours of real physical time are commonly adopted, particularly if storm conditions are of concern. In a laboratory context, this is possible by combining an efficient laboratory beach with actively absorbing wavemakers (Spinneken & Swan 2009*a*). The combination of these two measures eliminates the majority of the reflected wave content, and ensures a homogenous (and ergodic) sea state for a long testing duration.

In Numerical Wave Tanks (NWTs), downstream sponge layers or radiation conditions have long been established. Unfortunately, these cannot eliminate the reflections from a test model or structure back towards the wave generation boundary. To address this, active control on the numerical wave generation boundary has recently been introduced (Spinneken et al. 2013). This was achieved by implementing a technique established in the laboratory (force-feedback control) within a NWT. The purpose of the present paper is to advance the work by Spinneken et al. (2013), investigating the most efficient shape and control strategy for a NWT boundary.

The wavemaker in Spinneken et al. (2013) was chosen as a flap-type geometry; the reason for this choice being the compatibility to previous laboratory work. However, Naito (2006) and Maguire & Ingram (2011) showed that alternative geometries, usually based upon a cosh shape profile, may be significantly more efficient in achieving a broad-banded absorption characteristic. To test the wavemaker geometries introduced in Naito (2006) and Maguire & Ingram (2011), these are implemented in a fully-nonlinear NWT similar to that adopted in Spinneken et al. (2013). The main advance of the present work then lies in demonstrating that the analytical (or theoretical) concepts developed by Naito (2006) and Maguire & Ingram (2011) can also benefit a practical NWT implementation. A schematic representation of our two-dimensional NWT is given in Figure 1. Generation occurs on the left hand side, with absorption implemented on the right hand side. The cosh geometry indicated on this right hand side (Figure 1) illustrates that the absorbing condition makes use of the advantages of cosh-type velocities profiles.

The paper continues as follows. The first part outlines the principles of force based absorption in a NWT, and introduces the numerical scheme adopted. This is followed by a brief discussion concerning the wave field radiated by various wavemaker geometries, specifically addressing the linkage between the evanescent wave field, the added mass component, and the associated absorption control problem. Subsequently, the optimum absorption that can be achieved using a number of different wave board geometries is compared based on a set of analytical formulations. The validation of the work is then undertaken in three parts. First, the wavemaker hydrodynamic force is evaluated numeri-

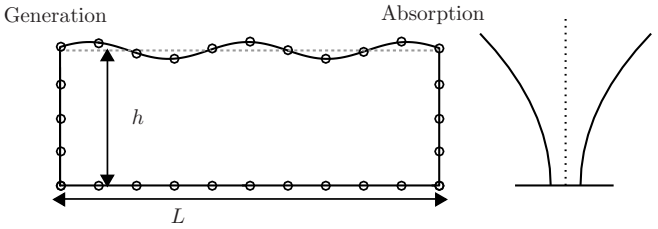


Figure 1: Numerical wave tank (left) and absorbing wavemaker geometry (right).

cally without any absorption feedback, which serves the validation of the force computation scheme in the NWT. Second, the absorption performance in regular waves is considered, where a number of wave board geometries and absorption controllers are contrasted. In a third validation step, the best available combination of wavemaker geometry and absorption controller is considered in random waves. The paper concludes by summarising the main findings, and offering suggestions for future work.

FORCE BASED WAVE ABSORPTION

Any physical or numerical wave tank relies on some form of wave generation and wave absorption boundaries. In physical wave tanks, a moving wavemaker introduces wave motion at the upstream generating boundary, and some form of passively absorbing beach is placed at the downstream end of the wave tank. To minimise re-reflections from physical models placed within the wave tank, the upstream wave generating boundary is now commonly designed as an absorbing wavemaker. A number of so-called 'double-ended' wave tanks also exist, where both wave flume ends (upstream and downstream) are fitted with active wave absorbers, which are capable of simultaneous generation and absorption. The operation of such 'double-ended' wave tanks has been reported in Spinneken & Swan (2009*b*) (physical wave tank) and Spinneken et al. (2013) (NWT).

The methodology reported in Spinneken & Swan (2009*b*) and Spinneken et al. (2013) builds upon force-feedback control using an IIR function for the purpose of the absorption controller. While other comparably efficient methodologies exist, the present contribution focuses on the operation using force-feedback control with an IIR filter approach. Alternative absorption methodologies are discussed in Milgram (1970), Salter (1982), Schäffer & Klopman (2000) and Naito (2006). A comparison between a number of different absorption strategies, including the present IIR approach, can be found in Spinneken & Swan (2009*c*). In essence, Spinneken & Swan (2009*c*) established that force-feedback control with IIR absorption filters is both robust and efficient, particularly because IIR filters are inherently causal, which overcomes the issues associated with a non-causal control problem as described in Falnes (1995).

Adopting force-based absorption relies on determining both the wavemaker velocity and the wavemaker force. The product of force and velocity (or torque and angular velocity for flap-type wavemakers) yields power, which in the case of optimum wave absorption is sought to be maximised. For a detailed description concerning the concepts of wave power absorption, the reader is referred to Evans (1976) and Falnes (1980). Assuming a single degree of freedom oscillator, the wavemaker in the present case, the total applied force F expressed in the frequency domain is given by

$$F = (M + m_r)(i\omega)^2 X + d_r i\omega X + \kappa X, \tag{1}$$

where X is the wavemaker displacement, M is the wavemaker mass, m_r is the added mass, d_r is the radiation damping, and κ is the buoyancy stiffness. Equation (1) leads to the definition of the dynamic wavemaker impedance as

$$Z_d = \frac{F}{U} = \frac{1}{(M + m_r)i\omega + d_r - i\kappa/\omega}, \tag{2}$$

where $U = i\omega X$ is the wavemaker velocity in the frequency domain. The dynamic wavemaker impedance Z_d has both real and imaginary components, where the former is driven by d_r and the latter is influenced by a combination of M, m_r and k. Optimum absorption control seeks to establish a controller or filter impedance $Z_f = Z_d^*$, where $*$ denotes the complex conjugate (Falnes 2002). The complex conjugate match ensures that both the phase and the magnitude conditions for optimum absorption are met, such that the absorber is under resonance. For a given absorption filter impedance Z_f, the power absorption coefficient may be derived

$$\gamma_p = 4\frac{\mathbb{R}(Z_f)\mathbb{R}(Z_d)}{\left[\mathbb{R}(Z_f) + \mathbb{R}(Z_d)\right]^2 + \left[\mathbb{I}(Z_f) + \mathbb{I}(Z_d)\right]^2}, \tag{3}$$

which is a well known result in electrical engineering, and has been shown for the absorbing wavemaker case in Spinneken & Swan (2009*a*). Based on the power absorption coefficient γ_p, the amplitude absorption coefficient may be obtained as $\gamma_a = 1 - \sqrt{1 - \gamma_p}$.

In practice, an IIR filter can be designed such that $Z_{IIR} \approx Z_f$, where the IIR coefficients (filter characteristics) are optimised to achieve Z_f as close as possible. The main difficulty in achieving $Z_{IIR} \approx Z_f$ lies in the fit at increasing wave frequencies ω. As ω increases, the term κ/ω decreases, and $(M + m_r)\omega$ increases. In fact, the buoyancy stiffness κ for numerical wavemakers is commonly assumed as zero, leading to $\kappa/\omega = 0$ for all ω. The total term $i((M + m_r)\omega - \kappa/\omega)$ hence becomes increasingly positive as ω increases. Given that $Z_f = Z_d^*$, the filter must now provide a negative imaginary part. While this is possible, in practice it becomes very difficult to design a filter which increases its imaginary part at the same rate as $(M + m_r)\omega$. Examples of difficulties of this type can be found in the optimum absorption filters shown in Spinneken & Swan (2009*a*), Spinneken & Swan (2009*c*) or Spinneken et al. (2013).

The present paper seeks to overcome this difficulty through geometric design of the wavemaker. In effect, the aim is to minimise the term $(M+m_r)\omega$. In the context of numerical wave generation, minimising the wavemaker mass is trivial, as the mass can simply be set to $M = 0$. Unfortunately, the added mass term m_r remains important, and its minimisation can only be achieved through geometric considerations. Attempts of this type have previously been reported in Maguire & Ingram (2011), where a number of different wavemaker geometries (piston, flap, cosh-shaped) were investigated, and the hydrodynamic coefficients were established analytically. While the work in Maguire & Ingram (2011) also investigated the theoretical absorption performance of these geometries, it did not actually demonstrate their use in either a physical or numerical wave tank. The purpose of the present work is to combine the findings of Maguire & Ingram (2011) with the NWT operation demonstrated in Spinneken et al. (2013).

In similarity to Spinneken et al. (2013), the formulation presented here relies on an implementation of a fully-nonlinear potential flow NWT. The NWT operates in the time domain, and retains the full nonlinearity of the free surface boundary conditions; a detailed description of the numerical scheme adopted being given in Spinneken et al. (2013). At this stage, it is important to note that the NWT adopts the so-called multiple-flux approach established by Hague & Swan (2009). Within the solution by Hague & Swan (2009), the corner problem that commonly arises in boundary element formulations is resolved by allowing for multiple fluxes at each of the computational nodes defining an intersection between two boundaries. In the present two-dimensional formulation, this allows for two normal fluxes at each intersection, which yields an accurate treatment of both the free surface and the wave generation boundary. The NWT will be referred to as MFBEM (Multiple-Flux Boundary Element Method) hereafter.

WAVE FIELD AND ADDED MASS

Wave absorption based on force control and IIR filters is commonly achieved using either flap-type or piston-type wavemakers. The present interest lies primarily in the practical performance that the IIR force based approach can offer for cosh shaped wavemakers. Nevertheless, to enable a direct comparison to previously established findings, results for common flap and piston geometries are also included.

Throughout the discussion of the theoretical concepts associated with optimum wave absorption, the mathematical expressions are introduced for linearised potential flow theory, where ϕ defines the velocity potential. Within a Cartesian coordinate system (x, z), the fluid velocity components are defined as $(u, w) = (\partial\phi/\partial x, \partial\phi/\partial z)$. The coordinate system is located such that $x = 0$ defines the mean location of the wavemaker, $z = 0$ defines the Still Water Level (SWL), and $z = -h$ defines the horizontal and impermeable bed. Mass continuity ensures that Laplace's equation, $\nabla^2\phi = 0$, is satisfied throughout the fluid. Furthermore, the standard boundary conditions for the wavemaking problem apply, where (a) the free surface is a streamline, giving rise to the kinematic free surface boundary condition, (b) the pressure on the free surface remains constant, giving rise to the dynamic free surface boundary condition, (c) the vertical fluid velocity along the horizontal and impermeable bed must be zero, and (d) the normal velocity of the fluid on the wavemaker must be equal to the wavemaker's velocity along that normal. Conditions (a)-(d) define a set of nonlinear boundary conditions, which is readily linearised and solved analytically for many wavemaker geometries. For brevity, the exact mathematical formulation is omitted here, and reference is made to the well established result of Dean & Dalrymple (1991). All important analytical expressions required here are summarised in Appendix A.

In defining the wave field arising due to the wavemaker motion, the wave field coefficient c_j is introduced such that the water surface elevation is given by

$$\eta = \mathbb{R}\left\{ iX_a \sum_{j=0}^{\infty} c_j \mathrm{e}^{\,i(\omega t - k_j x)} \right\}, \tag{4}$$

where X_a is the wavemaker displacement at the SWL, t denotes time and the wavenumber k_j is the solution to the generalised dispersion equation

$$\omega^2 = g k_j \tanh(k_j h), \tag{5}$$

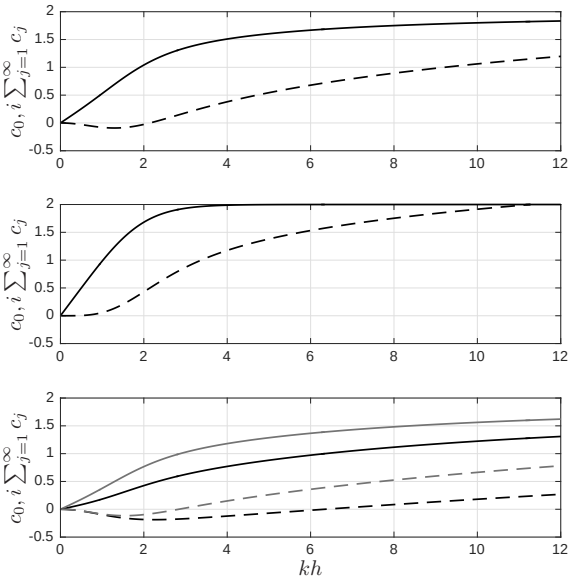


Figure 2: Wave field coefficients for flap-type wavemaker (top), piston-type wavemaker (centre) and cosh wavemaker (bottom), showing ——— progressive wave field coefficient c_0 and – – – sum of evanescent wave field coefficients $i\sum_{j=1}^{\infty} c_j$. For the cosh wavemaker (bottom part) both $\cosh_{\mathrm{A}}$ (grey line) and $\cosh_{\mathrm{B}}$ (black line) are shown.

where g denotes acceleration due to gravity. Adopting a compact complex notation, k_j is real for $j = 0$ and imaginary for $j \geq 1$. The first component, $j = 0$, defines a progressive water wave, while modes $j \geq 1$ define local standing (or evanescent) wave modes. Physically, the progressive wave mode is associated with the radiation damping term, and the local standing wave field ($j \geq 1$) governs the added mass component.

The wave field coefficients c_j in equation (4) may be solved analytically for a range of wavemaker geometries, including flap-type wavemakers, piston-type wavemakers and cosh profiles. For completeness, the wavemaker shape functions required to perform this analytical solution, as well as the resulting wave field coefficients c_j, are reported in Appendix A. Figure 2 shows the wave field coefficient for a flap-type wavemaker (top), a piston-type wavemaker (centre) and cosh shaped wavemakers (bottom). In each case, the solid line represents the coefficient c_0 and the dashed line gives the summation $i\sum_{j=1}^{J} c_j$, where $J = 50$. Beyond $J = 50$, the influence of additional wave modes is small and can be neglected.

The relation between the generated progressive wave amplitude, A, and c_j is given by $A = c_0 X_a$, which follows directly from equation (4). In effect, the progressive wave field coefficient c_0 expresses the ratio between the generated wave amplitude and the wavemaker displacement. In relatively shallow water ($kh < 1$), the piston wavemaker produces the largest wave amplitude for a given stroke (Figure 2), which is expected given the full-depth uniform velocity profile and the resulting displacement of fluid over the full water depth. In deeper water, c_0 for both the flap-type and the piston-type wavemakers approaches a limiting value of $c_0 = 2$, and the difference between the two geometries reduces in terms of progressive wave generation. For example, at $kh = 6$, the progressive wave field coefficient for the piston is only ap-

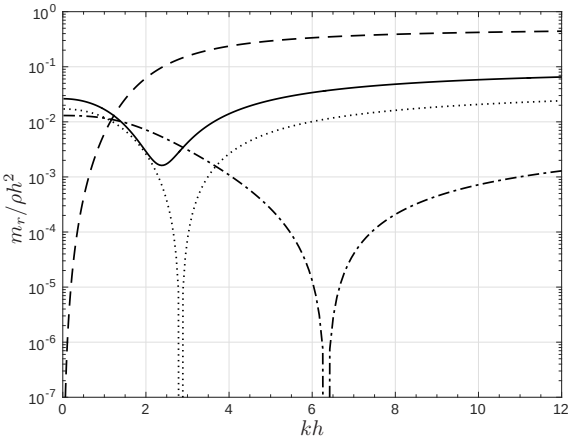


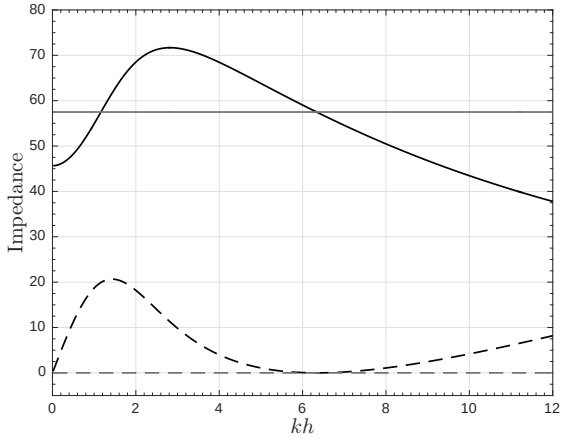
Figure 3: Added mass for wavemaker type ——— flap, – – – piston, ····· $\cosh_{\mathrm{A}}$ and –·–· $\cosh_{\mathrm{B}}$.

proximately 15% larger than that of the flap. In contrast, their evanescent mode behaviour in deep water is quite different. Again considering $kh = 6$, the piston evanescent wave field is more than twice that of the flap. Ultimately, as kh increases further, the evanescent wave field for both the flap-type and the piston-type wavemakers becomes increasingly more important, which leads to an increasing importance of the added mass term.

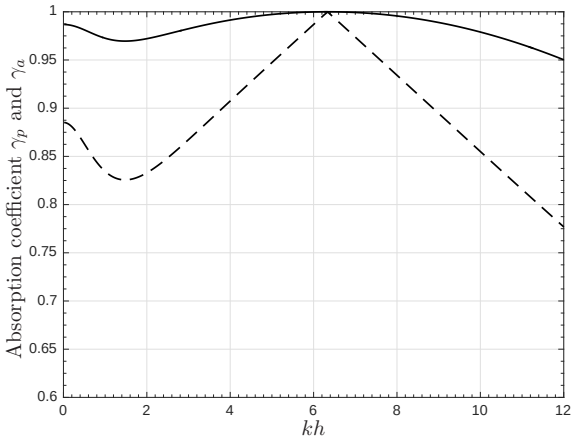
The cosh wavemakers illustrated in the bottom part of Figure 2 relate to two distinct geometries, each optimised such that its associated velocity profile matches a particular value of kh. Given that absorption becomes most challenging towards larger kh, the optimum values were chosen as $(kh)_{\mathrm{A}} = 2.8$ (referred to as $\cosh_{\mathrm{A}}$ hereafter) and $(kh)_{\mathrm{B}} = 6.3$ (referred to as $\cosh_{\mathrm{B}}$ hereafter). These two cosh shaped wavemakers show some distinctly different behaviour when compared to the piston-type or flap-type wavemakers. First, their progressive wave field coefficients are generally smaller, which implies that larger wavemaker strokes are required to generate comparable wave amplitudes. Furthermore, their standing wave field is reduced, and the term $i\sum_{j=1}^{J} c_j$ remains significantly smaller than c_0 for a wide range of kh.

Based on the observation of a reduced evanescent field, it is instructive to consider the added mass component for each wavemaker geometry; the analytical expressions adopted being given in Appendix A. Figure 3 contrasts the added mass for the four geometries introduced in Figure 2, where m_r is normalised as $m_r/\rho h^2$, and ρ is the density of the fluid. The piston-type wavemaker (dashed line) is found to have zero added mass at very low kh ($kh < 0.1$), which is expected given that the uniform velocity distribution along the wavemaker provides a near-perfect velocity match for the horizontal fluid velocity of a shallow water wave. The piston added mass increases rapidly with kh, a direct consequence of the fluid velocity mismatch at the wavemaker boundary, and reaches a near-constant value beyond $kh = 6$.

The added mass coefficients for the remaining three geometries are less straightforward in their behaviour. A distinct minimum is observed in all three cases (flap, $\cosh_{\mathrm{A}}$, $\cosh_{\mathrm{B}}$). For the cosh wavemaker geometries, the zero minimum arises when kh matches the optimum geometry. Away from the optimum frequency, the added mass increases, but remains smaller than the high-frequency value of the piston-type wavemaker. The flap-type wavemaker (solid line) also shows a minimum, but generally



(a) Impedance matching showing ——— $\mathbb{R}(Z_d)$, – – – $\mathbb{I}(Z_d)$, ——— $\mathbb{R}(Z_f)$, – – – $\mathbb{I}(Z_f)$.



(b) Absorption performance ——— power absorption coefficient, – – – amplitude absorption coefficient.

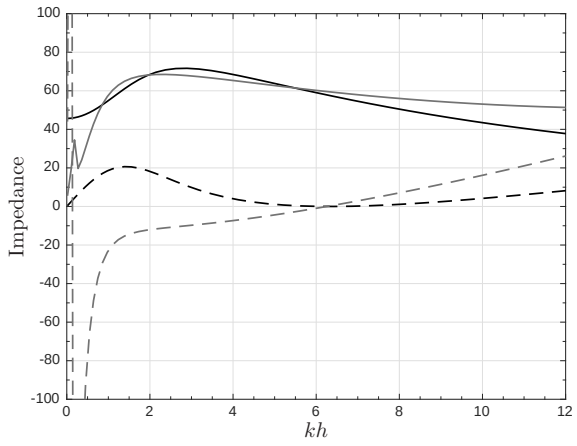
Figure 4: Optimum wave absorption for a $\cosh_{\mathrm{B}}$ wavemaker using a simple proportional gain absorption controller with (a) Impedance matching and (b) Absorption performance

exhibits larger values than the cosh shaped geometries.

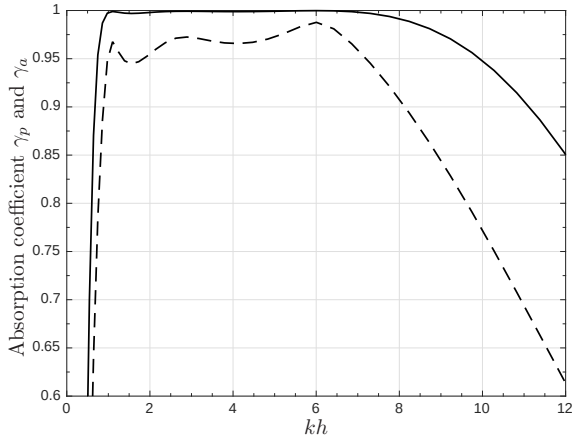
OPTIMUM WAVE ABSORPTION

Figures 4 and 5 show the absorption characteristics for a $\cosh_{\mathrm{B}}$ wavemaker, where part (a) illustrates the impedance matching procedure and part (b) relates to the absorption performance. The impedance matching illustrated in Figures 4(a) and 5(a) contains four components: (i) the real part of the dynamic wavemaker impedance $\mathbb{R}(Z_d)$ (black solid line), (ii) the corresponding imaginary part $\mathbb{I}(Z_d)$ (black dashed line), (iii) the real part of the filter impedance $\mathbb{R}(Z_f)$ (grey solid line) and (iv) the imaginary part of the filter impedance $\mathbb{I}(Z_d)$ (grey dashed line). The absorption performance in Figures 4(b) and 5(b) illustrates both the power absorption coefficient γ_p (solid line) and the amplitude absorption coefficient γ_a (dashed line).

The absorption controller in Figure 4 is based on a simple proportional gain control, which is similar to the controllers presented in Maguire & Ingram (2011). The proportional gain is directly applied to the wavemaker velocity, and results in a constant real part $\mathbb{R}(Z_f)$ and zero imaginary part $\mathbb{I}(Z_f)$ for the filter in



(a) Impedance matching showing $\mathbb{R}(Z_d)$, $\mathbb{I}(Z_d)$, $\mathbb{R}(Z_f)$, $\mathbb{I}(Z_f)$.



(b) Absorption performance power absorption coefficient, amplitude absorption coefficient.

Figure 5: Optimum wave absorption for a $\cosh_{\mathrm{B}}$ wavemaker using an IIR filter approach with (a) Impedance matching and (b) Absorption performance

Figure 4(a). At the optimum frequency of the $\cosh_{\mathrm{B}}$ wavemaker, the evanescent wave field vanishes, such that the imaginary part of the wavemaker impedance, $\mathbb{I}(Z_d)$, also vanishes (dashed line in Figure 4(a)). The proportional gain is set such that it matches the real part of the wavemaker impedance at the optimum frequency. Given that both the real part and the imaginary part match exactly at the optimum frequency, perfect absorption can be achieved as evident in Figure 4(b) where both $\gamma_p = \gamma_a = 1$ at $kh = 6.3$. Unfortunately, at frequencies away from the single optimum frequency, the absorption performance deteriorates rapidly, and the absorption performance can be classified as very narrow banded.

To achieve a much more broad banded performance, the absorption controller in Figure 5 is based on a more complex IIR filter approach. Figure 5(a) demonstrates that both the real and the conjugate imaginary parts of the absorption filter match the characteristics of the wavemaker over a broad range of kh. The improved match is directly evident in Figure 5(b), where the amplitude absorption coefficient is in excess of 90% for $1 \leq kh \leq 8$, with a power absorption coefficient near unity over this range. Indeed, in comparing the absorption performance in Figure 5 to previously reported results for flap-type or piston-type wavemakers (Spinneken & Swan 2009*a*, Spinneken & Swan 2009*b*, Spinneken et al. 2013), a significant improvement in terms of absorption bandwidth can be observed. Due to the moderate increase of the added mass term m_r as kh increases, the overall absorption performance of the cosh wavemaker remains very high even in deep water (large kh). While this result is as expected, Figure 5 represents the first ever reported IIR filter performance for a cosh shaped wavemaker.

VALIDATION OF A COSH WAVEMAKER IN A NWT

Having established that the cosh shaped wavemaker can serve as an excellent broad-banded wave absorber if based on the IIR filter approach, the cosh geometry was implemented in the MF-BEM NWT. The absorption performance achieved in practice depends upon the underlying hydrodynamic properties of the wavemaker, including c_j, m_r, d_r and F. The purpose of the present section is to validate that the wavemaker performs as expected. To achieve this, a number of regular wave cases lying in the range $1.5 \leq kh \leq 11$ were generated within the NWT, and comparisons were made to the linear analytical formulation. To ensue that the NWT results lie within the linear or small-amplitude regime, the wave steepness for all cases was kept at $Ak_0 = 0.01$.

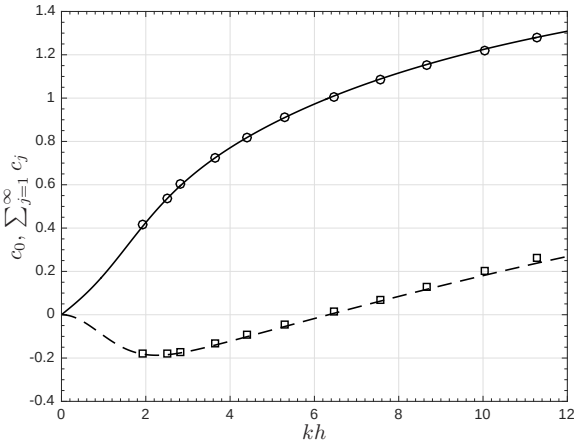
The results of the initial NWT validation are presented in Figure 6, where the three parts relate to (a) the wave field coefficient c_j, (b) the magnitude of the normalised radiation force $|F|/\rho g X_a h$ and (c) the phase angle of the radiation force $\arg(F)$. Figure 6(a) shows both the progressive wave field coefficient c_0 (solid line) and the evanescent wave field $\sum_{j=1}^{\infty} c_j$. To obtain the wave field coefficients from the NWT simulation, the following procedure was adopted:

(i) The water surface elevation of the generated wave field under steady-state conditions was recorded at $x = 3h$, where the wave field can be assumed as free from evanescent modes. Performing a Discrete Fourier Transform (DFT) on the time-history of the surface elevation at $x = 3h$ yields the progressive wave amplitude A. Dividing this wave amplitude by the known wavemaker displacement X_a yields the coefficient c_0. The agreement between the NWT result and the analytical solution observed in Figure 6(a) is excellent for all kh.

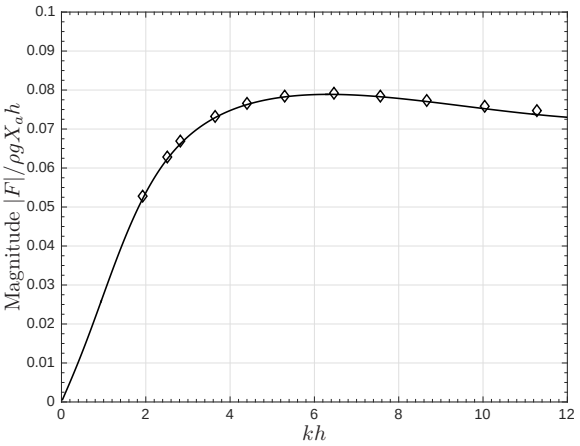
(ii) A DFT was applied to the water surface elevation at $x = 0$. Given that $\mathrm{e}^{ik_j x}$ at $x = 0$ is unity for all k_j, the evanescent wave field is fully established at this location. Subtracting the progressive wave amplitude from the total amplitude at $x = 0$ yields the evanescent wave amplitude. Dividing by X_a as before gives the total sum of $\sum_{j=1}^{\infty} c_j$. The agreement between the NWT data and the analytical solution is very good (Figure 6(a)), with some small departures in very deep water (large kh). These departures are due to insufficient spatial resolution in the NWT (Spinneken et al. 2013) and can be overcome by increasing Δx.

The force magnitude and phase shown in Figure 6(b) and 6(c) were obtained as follows. The total pressure at any point in the fluid domain is given by the unsteady form of Bernoulli's equation as

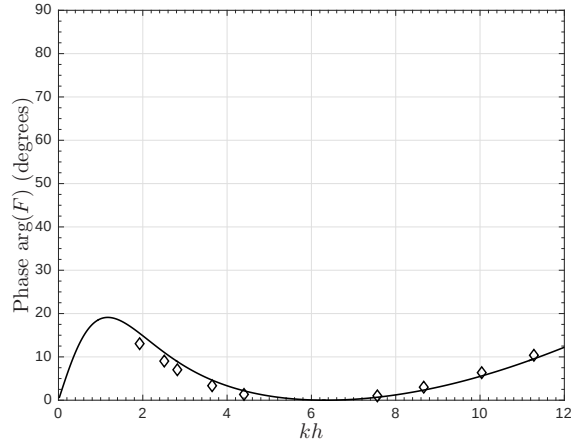
$$p = -\rho \frac{\partial \phi}{\partial t} - \rho g z - \frac{1}{2}\left(\left(\frac{\partial \phi}{\partial x}\right)^2 + \left(\frac{\partial \phi}{\partial z}\right)^2\right), \tag{6}$$



(a) Wave field coefficients showing ——— analytical solution for c_0, – – – analytical solution for c_j, ∘ NWT data for c_0 and □ NWT data for c_j.



(b) Magnitude of the total radiation force with ——— analytical solution and ⋄ NWT data.



(c) Phase of the total radiation force with ——— analytical solution and ⋄ NWT data.

Figure 6: Validation of the $\cosh_B$ wavemaker in a NWT showing (a) wave field coefficient (b) force magnitude and (c) force phase.

and the force is computed by integrating this pressure over the surface of the wavemaker. The second and the third term on the right hand side of equation (6) are readily computed based on the MFBEM scheme introduced by Hague & Swan (2009). Evaluating the term $\partial\phi/\partial t$ along a solid boundary can be challenging, particularly if the floating body behaviour or active absorption control is required (Kashiwagi 2000, Spinneken et al. 2013). The reason for this lies in the fact that a simple backward difference scheme for $\partial\phi/\partial t$ is often reported to lead to numerical instabilities when the term is used to feed-back into the simulation. For the example of a floating body, the forcing due to $\partial\phi/\partial t$ affects the body acceleration, which in turn affects the body velocity and hence the fluid velocity. The fluid velocity feeds back into the velocity potential and hence also $\partial\phi/\partial t$. As a result, any problems in evaluating $\partial\phi/\partial t$ also affect the global simulation. To overcome the issues of numerical instability for this type of coupling, both Kashiwagi (2000) and Spinneken et al. (2013) used the so-called indirect method, which avoids the use of a backwards difference by formulating a second Boundary Value Problem (BVP) in terms of $\partial\phi/\partial t$.

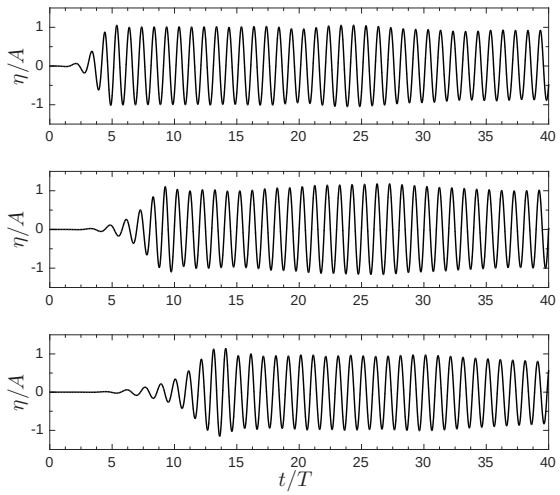
Nevertheless, for the purpose of the present investigation, the simple backwards difference scheme is employed; the reasons for this choice being as follows. In floating body dynamics, the hydrodynamic force directly leads to the computation of the body acceleration. In contrast, the hydrodynamic force here enters a motion controller which contains an integrator. The integrator ensures that any instabilities (or high frequency noise) arising in the differentiation is smoothed. For the avoidance of any doubt, this smoothing effect is not introduced artificially, but is an essential element of the wavemaker's motion controller.

From Figure 6 is it clear that the force computation based on a backwards difference scheme yields very good agreement in terms of both the magnitude of F (Figure 6(a)) and its phase (Figure 6(b)). In considering Figure 6(c), is should be noted that the phasing behaviour is closely related to the added mass behaviour, Figure 3. At the frequency of zero added mass in the vicinity of $kh = 6.3$, the phase of the radiation force is also zero, and the force is dominated by the radiation damping term. The fact that the phase remains under 20 degrees for most values of kh indicates that the added mass only plays a very minor role in the overall wavemaker forcing. This is in marked contrast to flap-type or piston-type wavemakers, where the forcing is dominated by the added mass at large kh (Spinneken et al. 2013).

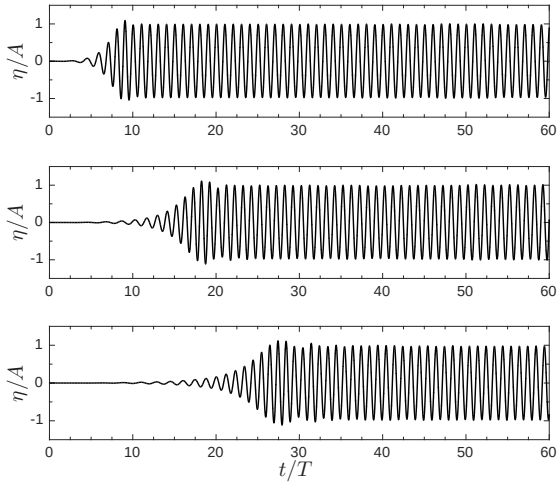
WAVE ABSORPTION IN REGULAR WAVES

This section presents, for the first time, the absorption performance of cosh shaped wavemakers in a time-domain NWT. The NWT is of length L and depth h as previously illustrated in Figure 1. On the left hand side (or upstream) boundary, regular waves are generated by imposing a fluid velocity that exactly matches that of the desired progressive wave. On the right hand side (or downstream) boundary, an absorbing cosh shaped wavemaker is installed.

The first two test cases, presented in Figure 7, relate to the simple proportional filter based on the characteristics previously shown in Figure 4. This particular controller applies a proportional gain to the wavemaker velocity, with no imaginary part in the filter impedance (Figure 4(a)). The controller operates most efficiently at a frequency of $kh = 6.3$ ($\cosh_B$ wavemaker), where the added mass term of the wavemaker is zero. Figure 7 relates to a regular wave frequency of (a) $kh = 2.8$ and (b) $kh = 6.3$,



(a) Wave case with $kh = 2.8$



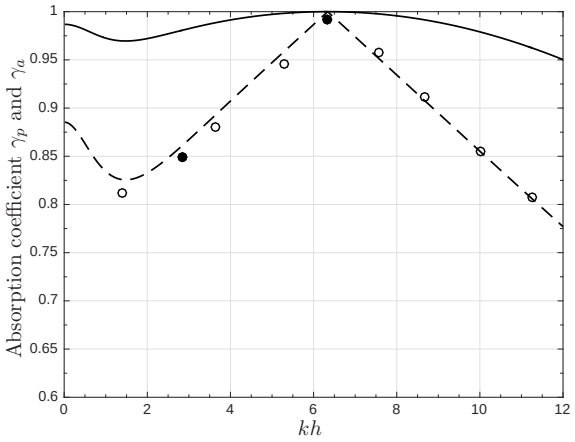
(b) Wave case with $kh = 6.3$

Figure 7: Water surface elevation $\eta(t)$ recorded at $x = 3h$ (top), $x = L/2$ (centre) and $x = L-3h$ (bottom) using a simple proportional controller with a $\cosh_{\mathrm{B}}$ wavemaker optimised at $kh = 6.3$.

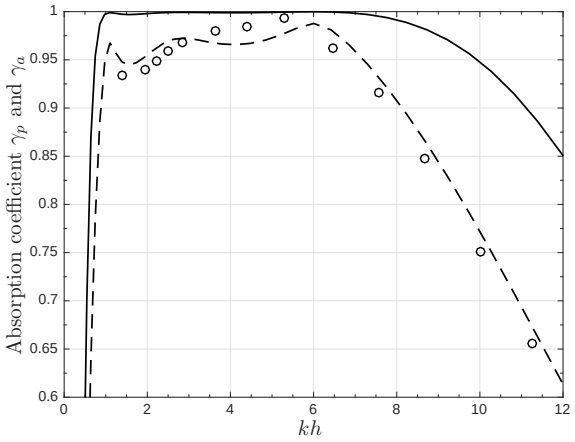
where the latter represents the wavemaker's optimum frequency. The time-history of the water surface elevation is shown at three spatial locations: $x = 3h$ (top), $x = L/2$ (centre) and $x = L - 3h$ (bottom); a distance of $3h$ from either the upstream or the downstream boundary being chosen to avoid evanescent waves[1].

In considering the surface elevation in Figure 7, it should be noted again that the present MFBEM computation scheme operates in the time domain, which includes the transient response of the fluid as the wave propagates into initially still water conditions. Following the initial transient response, a condition of perfect absorption is characterised by a normalised water surface elevation η/A of unity at all times and locations. The NWT tank adopted for the test case in Figure 7 is relatively short, such that any reflections arising at the downstream boundary quickly

[1]In practice, the evanescent wave field of the upstream boundary is zero, as the exact velocity profile is imposed for each wave case. However, the downstream absorbing boundary is only evanescent wave free at $kh = 6.3$, and contains evanescent waves away from this frequency.



(a) Controller with simple proportional gain



(b) Controller with optimised IIR filter

Figure 8: Numerically observed amplitude absorption coefficient (symbol ∘) compared to theoretically established characteristics showing ——— power absorption coefficient, – – – amplitude absorption coefficient.

contaminate the wave tank. Considering the surface elevation in Figure 7(a) it is clear that η/A deviates significantly from unity as time progresses. Close to the downstream boundary (bottom part of Figure 7(a)), reflections are apparent almost immediately after the wave reaches this location. The reflections reach the upstream boundary (top) at $t/T \approx 24$, and re-reflections from the upstream boundary can be observed at both the NWT centre ($t/T \approx 30$) and the downstream location ($t/T \approx 36$). If the NWT simulation was continued, ever more wave reflections would build up, rendering long testing impractical. While long testing would almost certainly not be required in the case of regular waves, significant test durations are essential to random waves as discussed further below.

From the surface elevation shown in Figure 7(b), it can be concluded that very little wave reflections enter the numerical domain for a regular wave case with $kh = 6.3$. Indeed, the normalised water surface elevation η/A remains very close to unity once the initial transient part of the wave profile, due to propagation into initially still water, has passed. This is as expected, given that $kh = 6.3$ relates to the optimum wavemaker absorption case for this configuration of shape ($\cosh_{\mathrm{B}}$) and controller (simple

proportional gain). To quantify the extent of the wave absorption for a wider range of test cases, Figure 8 presents the numerically observed amplitude absorption coefficient (discrete circles), where the theoretically established behaviour is also shown. Figure 8(a) corresponds to the simple proportional controller, and the two test cases discussed in Figure 7 are highlighted using the symbol •.

Figure 8(a) demonstrates that the actual NWT implementation for a cosh shaped wavemaker operates effectively and closely matches the theoretical prediction. Absorbing cosh wavemakers have not been implemented in time domain NWT schemes before, and the data in Figure 8 presents an important advance of the present investigation. Importantly, the good match between the theoretical performance and the NWT data can also be observed for the IIR based absorption controller shown in Figure 8(b). For this controller, the amplitude absorption coefficient remains above 90% (or 99% power absorption) for the range $1 \leq kh \leq 8$, which covers the vast majority of wave components expected in a realistic offshore spectrum. Some small discrepancies remain between the NWT data and the theoretical absorption performance. These can be due to a number of causes, most likely the effect of limited loop gain in the force-feedback control loop. Improved closed-loop control forms an important part of our ongoing work, but is outside the scope of the present investigation. Nevertheless, the NWT absorption behaviour shown in Figure 8(b) is among the very best ever reported in the literature, and does not in any way rely on a sponge layer.

WAVE ABSORPTION IN IRREGULAR WAVES

Having established the success of the absorption controller in regular waves, the performance of the IIR / cosh approach is now considered in irregular waves. For this purpose, a wave spectrum with an underlying JONSWAP energy density function is generated on the upstream boundary using the second-order fluid velocities provided by Sharma & Dean (1981). The absorbing wavemaker is placed on the downstream boundary as before. The sea state is discretised into a finite number of frequency components, which are chosen such that all components are periodic in a repeat time T_r. As a result, the entire sea state is also periodic in T_r. The sea state peak frequency is chosen as $k_p h = 1.6$, and a relatively small amplitude sea state with $\frac{1}{2} H_s k_p = 0.01$ is considered, where H_s is the significant wave height.

Figure 9 shows the normalised water surface elevation, $\eta(t)/H_s$, recorded at $x = 3h$ (top), $x = L/4$ (centre) and $x = L/2$ (bottom). In each case, the surface elevation shown corresponds to two distinct time intervals. First, the solid grey line relates to $0 \leq t/T_r \leq 1$ and, second, the dashed black line relates to $1 \leq t/T_r \leq 2$, where the latter has been time shifted by T_r to enable a direct comparison to the former. To be entirely clear, the surface elevations presented in each part of Figure 9 correspond to one continuous simulation of total duration $2T_r$.

The water surface elevation during the interval $0 \leq t/T_r \leq 1$ is initially characterised by wave propagation into still water conditions. Naturally, this effect is more pronounced at distances further away from the upstream wavemaker (increasing x). From approximately $t/T_r = 0.5$, the surface elevation is fully established at all three measurement locations. The length of the NWT domain L was chosen such that the recording in the first interval at locations $x \leq L/2$ is free from wave reflections. However, wave reflections from the downstream boundary would affect the recording in the second time interval. The near-perfect

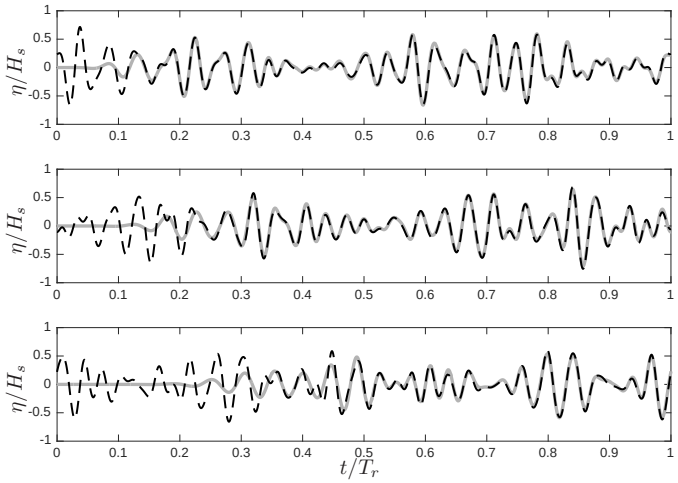


Figure 9: Water surface elevation $\eta(t)/H_s$ for a random sea state with $k_p h = 1.6$ observed at $x = 3h$ (top), $x = L/4$ (centre) and $x = L/2$ (bottom) showing recordings in the time intervals ——— $0 \leq t/T_r \leq 1$ and – – – $1 \leq t/T_r \leq 2$, where the latter has been shifted by T_r to enable a direct comparison to the former.

match between the two intervals indicates that reflected waves are largely absent, providing evidence of the success of the absorption mechanism in irregular waves.

CONCLUSIONS

The present investigation has considered the absorption performance that can be achieved with cosh wavemakers and IIR absorption filters. An optimum IIR filter was designed that makes full use of the cosh wavemaker's low added mass term at high frequencies. The main aim of the filter optimisation was to achieve a broad banded absorption behaviour, suitable for the application to realistic ocean wave spectra. Based on the optimum IIR filter, the cosh shaped wavemaker was shown to exhibit a very broad absorption response, yielding in excess of 90% amplitude absorption in the range $1 \leq kh \leq 8$. A broad banded behaviour of this type is significantly better than what can be achieved based on a simple proportional gain absorption controller. The cosh wavemaker / IIR filter combination was also tested in an irregular sea state, where an observation of the water surface elevation confirmed the success of the absorption mechanism. Ongoing work concerns the wave crest statistics arising in long repeat times equivalent to 3-hour sea states, and these will be reported in the near future.

REFERENCES

Dean, R. & Dalrymple, R. (1991), *Water Wave Mechanics for Engineers and Scientists*, World Scientific.

Evans, D. (1976), 'A theory for wave-power absorption by oscillating bodies', *Journal of Fluid Mechanics* **77**, 1–25.

Falnes, J. (1980), 'Radiation impedances matrix and optimum power absorption for interacting oscillators in surface waves', *Applied Ocean Research* **2**(2), 75–80.

Falnes, J. (1995), 'On non-causal impulse response functions related to propagating water waves', *Applied Ocean Research* **17**, 379–389.

Falnes, J. (2002), *Ocean Waves and Oscillating Systems*, Cambridge University Press.

Hague, C. & Swan, C. (2009), 'A multiple flux boundary element method applied to the description of surface water waves', *Journal of Computational Physics* **228**(14), 5111 – 5128.

Kashiwagi, M. (2000), 'Non-linear simulations of wave-induced motions of a floating body by means of the mixed eulerian-lagrangian method', *Proceedings of the Institution of Mechanical Engineers, Part C: Journal of Mechanical Engineering* **214**(6), 841 – 855.

Latheef, M. & Swan, C. (2013), 'A laboratory study of wave crest statistics and the role of directional spreading', *Proceedings of the Royal Society A-Mathematical Physical and Engineering Sciences* **469**.

Maguire, A. & Ingram, D. (2011), 'On geometric design considerations and control methodologies for absorbing wavemakers', *Journal of Coastal Engineering* **58**, 135–142.

Milgram, J. (1970), 'Active water-wave absorbers', *Journal of Fluid Mechanics* **43**, 845–859.

Naito, S. (2006), 'Wave generation and absorption in wave basins: Theory and applications', *International Journal of Offshore and Polar Engineering* **16**(2), 81–89.

Rodríguez, M. & Spinneken, J. (2016), 'A laboratory study on the loading and motion of a heaving box', *Journal of Fluids and Structures (under review)* .

Salter, S. (1982), Absorbing wave-makers and wide tanks, *in* 'Directional Wave Spectra Applications', pp. 185–200.

Schäffer, H. (1996), 'Second-order wavemaker theory for irregular waves', *Ocean Engineering* **23**, 47–88.

Schäffer, H. & Klopman, G. (2000), 'Review of multidirectional active wave absorption methods', *Journal of Waterway, Port, Coastal and Ocean Engineering* **126**(2), 88 – 97.

Sharma, J. N. & Dean, R. G. (1981), 'Second-order directional seas and associated wave forces', *Society of Petroleum Engineering* **4**, 129–140.

Spinneken, J. (2010), Wave generation and absorption using force-feedback control, Phd thesis, Imperial College London.

Spinneken, J., Christou, M. & Swan, C. (2013), 'Force-controlled absorption in a fully-nonlinear numerical wavetank.', *Journal of Computational Physics* **272**, 127–148.

Spinneken, J. & Swan, C. (2009*a*), 'Second-order wave maker theory using force-feedback control. Part I: A new theory for regular wave generation', *Ocean Engineering* **36**(8), 539 – 548.

Spinneken, J. & Swan, C. (2009*b*), 'Second-order wave maker theory using force-feedback control. Part II: An experimental verification of regular wave generation', *Ocean Engineering* **36**(8), 549 – 555.

Spinneken, J. & Swan, C. (2009*c*), Wave generation and absorption using force-controlled wave machines, *in* 'Proceedings of the 19th International Offshore and Polar Engineering Conference', Vol. 3, pp. 397–404.

APPENDIX A - HYDRODYNAMIC COEFFICIENTS

The purpose of this appendix is to provide all analytical expressions relevant to the present investigation, including the wave field coefficients as well as the hydrodynamic coefficients. Expressions are provided for the piston-type, flap-type and cosh shaped wavemakers. The coefficients c_j, linking the wave board motion to the generated wave field may be derived by solving the BVP for each particular geometry. To achieve this, the shape function for each wavemaker, $f(z)$, must be defined. These shape functions are as follows

$$f(z) = \begin{cases} 1 & \text{for a piston-type} \\ 1 + \frac{z}{h} & \text{for a flap-type} \\ \frac{\cosh(k_{0,\mathrm{wm}}(h+z))}{\cosh(k_{0,\mathrm{wm}}h)} & \text{for a cosh shape} \end{cases} \tag{A1}$$

where $k_{0,\mathrm{wm}}$ defines the wavenumber that is used to determine the optimum shape of the wave board.

Following the derivations in Schäffer (1996), the wave field coefficients for the piston-type and flap-type wavemakers are

$$c_j = \frac{2\sinh^2(k_j h)}{k_j h + \sinh(k_j h)\cosh(k_j h)} \tag{A2}$$

and

$$c_j = 2\sinh(k_j h)\frac{\sinh(k_j h) + (1-\cosh(k_j h))/(k_j h)}{k_j h + \sinh(k_j h)\cosh(k_j h)}. \tag{A3}$$

respectively. The cosh wavemaker is defined by

$$c_j = \frac{2\sinh(k_j h)k_j\left[k_j\sinh(k_j h) - k_{0,\mathrm{wm}}\cosh(k_j h)\tanh(k_{0,\mathrm{wm}}h)\right]}{\left(k_j h + \cosh(k_j h)\sinh(k_j h)\right)\left(k_j^2 - k_{0,\mathrm{wm}}^2\right)} \tag{A4}$$

if $k_0 \neq k_{0,\mathrm{wm}}$ and

$$c_j = \tanh(k_{0,\mathrm{wm}}h) \tag{A5}$$

if $k_0 = k_{0,\mathrm{wm}}$ and $j = 0$, which is consistent with Naito (2006). Following the work by Spinneken (2010), the radiation hydrodynamic coefficients for the piston-type wavemaker are given by

$$d_r = \frac{\rho g}{\omega}\frac{c_0}{k_0}\tanh(k_0 h) \tag{A6}$$

and

$$m_r = -i\frac{\rho g}{\omega^2}\sum_{j=1}^{\infty}\frac{c_j}{k_j}\tanh(k_j h) \tag{A7}$$

In close similarity, the hydrodynamic coefficients for a bottom-hinged flap-type wavemaker undergoing a rotational motion[2] may be obtained as

$$d_r = \frac{\rho g h}{\omega}\frac{c_0}{k_0^2}\frac{k_0 h\sinh(k_0 h) - \cosh(k_0 h) + 1}{\cosh(k_0 h)} \tag{A8}$$

and

$$m_r = -i\frac{\rho g h}{\omega^2}\sum_{j=1}^{\infty}\frac{c_j}{k_j^2}\frac{k_j h\sinh(k_j h) - \cosh(k_j h) + 1}{\cosh(k_j h)} \tag{A9}$$

Adopting the same notation as Spinneken (2010), but following the underlying equations outlined in Falnes (2002), the radiation damping for a cosh wavemaker is given by

$$d_r = \frac{\rho g}{\omega}\frac{c_0\left[k_0\tanh(k_0 h) - k_{0,\mathrm{wm}}\tanh(k_{0,\mathrm{wm}}h)\right]}{k_0^2 - k_{0,\mathrm{wm}}^2} \tag{A10}$$

if $k_0 \neq k_{0,\mathrm{wm}}$ and

$$d_r = \frac{1}{2}\frac{\rho g}{\omega}\frac{c_0}{k_0}\frac{k_0 h + \sinh(k_0 h)\cosh(k_0 h)}{\cosh^2(k_0 h)} \tag{A11}$$

if $k_0 = k_{0,\mathrm{wm}}$. The added mass for the cosh wavemaker is defined as

$$m_r = -i\frac{\rho g}{\omega^2}\sum_{j=1}^{\infty}\frac{c_j\left[k_j\tanh(k_j h) - k_{0,\mathrm{wm}}\tanh(k_{0,\mathrm{wm}}h)\right]}{k_j^2 - k_{0,\mathrm{wm}}^2} \tag{A12}$$

[2]Note: The added mass for the flap-type wavemaker in Figure 3 has been divided by h^2 when compared to the analytical expression given here. The factor h^2 arises in translating the horizontal wavemaker force to a torque around the wavemaker hinge. The comparison in Figure 3 is based on the horizontal force rather than the torque.